

Numerical experiments on magnetic reconnection in solar flare and coronal mass ejection current sheets

Z. Mei,^{1,2★} C. Shen,^{1,2,3} N. Wu,⁴ J. Lin,^{1,3★} N. A. Murphy³ and I. I. Roussev^{1,5}

¹Yunnan Astronomical Observatory, Chinese Academy of Sciences, PO Box 110, Kunming, Yunnan 650011, China

²Graduate School of the Chinese Academy of Sciences, Beijing 100049, China

³Harvard–Smithsonian Center for Astrophysics, 60 Garden Street, Cambridge, MA 02138, USA

⁴School of Tourism and Geography, Yunnan Normal University, Kunming, Yunnan 650031, China

⁵Institute for Astronomy, University of Hawaii, 2680 Woodlawn Dr, Honolulu, HI 96822, USA

Accepted 2012 June 26. Received 2012 June 26; in original form 2012 April 13

ABSTRACT

Magnetic reconnection plays a critical role in energy conversion during solar eruptions. This paper presents a set of magnetohydrodynamic experiments for the magnetic reconnection process in a current sheet (CS) formed in the wake of the rising flux rope. The eruption results from the loss of equilibrium in a magnetic configuration that includes a current-carrying flux rope, representing a pre-existing filament. In order to study the fine structure and micro processes inside the CS, mesh refinement is used to reduce the numerical diffusion. We start with a uniform, explicitly defined resistivity which results in a Lundquist number $S = 10^4$ in the vicinity of CS. The use of mesh refinement allows the simulation to capture high-resolution features such as plasmoids from the tearing mode and plasmoid instability regions of turbulence and slow-mode shocks. Inside the CS, magnetic reconnection goes through the Sweet–Parker and the fractal stages, and eventually displays a time-dependent Petschek pattern. Our results support the concept of fractal reconnection suggested by Shibata et al. and Shibata & Tanuma, and also suggest that the CS evolves through Sweet–Parker reconnection prior to the fast reconnection stage. For the first time, the detailed features and/or fine structures inside the coronal mass ejection/flare CS in the eruption were investigated in this work.

Key words: instabilities – magnetic reconnection – shock waves – turbulence – Sun: coronal mass ejections (CMEs) – Sun: flares.

1 INTRODUCTION

Magnetic reconnection is at the core of many dynamic phenomena in the universe, including solar eruptions, geomagnetic substorms and tokamak disruptions. Most of the universe is in the form of a plasma threaded by a magnetic field. When twisted or sheared, the field lines may reconnect rapidly, converting magnetic energy into heat and kinetic energy (e.g. Priest & Forbes 2000). Because these phenomena often occur in environments of very high electric conductivity, the process of energy conversion is usually confined to a small local region, such as an X-type neutral point, a current sheet (CS) or a quasi-separatrix layer (e.g. see also the review by Priest & Forbes 2002).

To allow major eruptions to continue, the reconnection process generally needs to occur at a reasonably fast rate. This gener-

ally implies that the reconnection region must have structure on scales smaller than the ion inertial length or the proton sound Larmor radius, which are tens to hundreds of metres in the corona (Litvinenko 1996; Wood & Neukirch 2005 and references therein). On these scales, collisionless effects lead to fast reconnection as observed in near-Earth space plasmas (e.g. Øieroset et al. 2001) and in dedicated laboratory experiments (e.g. Yamada et al. 2006). A key question during solar eruptions is how structure on these short length scales is able to develop while the overall observed thickness is orders of magnitude larger.

However, the coronal mass ejection (CME)/flare CS forms and develops very rapidly during a solar eruption. Theoretical calculations (e.g. Forbes & Lin 2000; Lin & Forbes 2000; Lin 2002) indicate that the CS in the major eruptive process could evolve and extend in length at speeds up to 10^2 km s^{-1} , and observational results of Ko et al. (2003) and Lin et al. (2005) suggest that the CS rapidly evolves as well. In such a highly dynamical process, the scale, especially the thickness, of a CS should not be as simple as

*E-mail: meizhixing@yao.ac.cn (ZM); jlin@yao.ac.cn (JL)

the Larmor radius of particles. Instead, various plasma instabilities must occur and play an important role in governing the CS scale (Strauss 1988; Drake et al. 2006).

Among these instabilities, the tearing mode, together with the consequent plasmoid instability (e.g. see Loureiro, Schekochihin & Cowley 2007; Bhattacharjee et al. 2009; Huang, Bhattacharjee & Zweibel 2010), is the most important one. Here the formation of plasmoids is considered as a non-linear stage of the classical tearing mode instability, which was referred by Bhattacharjee et al. (2009) to the super-Alfvénic tearing mode instability or the plasmoid instability. The excess resistivity caused by the turbulence as a result of the instability tremendously enhances the diffusion of the magnetic field (Strauss 1988; Bhattacharjee & Yuan 1995), and the turbulence also provides an excess pressure inside the CS helping balance the pressure outside by the reconnection inflow. Plasma blobs observed in the sheet (e.g. see Ko et al. 2003; Lin et al. 2005; Savage et al. 2010) indicate that the magnetic reconnection process is turbulent, and thus allowing the energy conversion to process at fairly quick speed in a thick CS.

In numerical experiments, the formation and evolution of plasma blobs in the CME/flare CS have also been noticed for decades. The results of Forbes & Malherbe (1991) and Riley et al. (2007) suggested that the tearing mode instability plays an important role in magnetic diffusion and governs the CS scale. Shen, Lin & Murphy (2011) showed that the reconnection process became fast and the thickness of the sheet remained roughly constant following the appearance of small-scale structure in the CS. The power-law distribution of the energy versus the scale of small features inside the CS displayed by Bárta et al. (2011) further depicted a scenario of the turbulent reconnection.

However, the gap between these experiments and actual major solar eruptions is also apparent. Those by Forbes & Malherbe (1991), Bárta, Vršnak & Karlický (2008), Karlický & Bárta (2011), Bárta et al. (2011) and Shen et al. (2011) are for the scenario of the Kopp–Pneuman two-ribbon flare, in which the CME is supposed to be at infinity; those by Loureiro et al. (2005), Huang et al. (2010), Murphy (2010) and Murphy, Sovinec & Cassak (2010) are more likely for the cases occurring in the lab or for the pure theoretical studies; and that by Riley et al. (2007) does include both flare and CME, but it does not reveal enough details inside the sheet.

In the present work, we investigate the fine structure inside the CME/flare CS, investigating the impact of these structures on the process of magnetic reconnection, and look into the implication of these manifestations to the physical properties of various processes occurring in the sheet. We construct a numerical version of the catastrophe model on the basis of the work by Isenberg, Forbes & Demoulin (1993), in which a current-carrying flux rope is included and is used to model the filament, and the background field is equivalent to that produced by a submerged, two-dimensional magnetic quadrupole. A gravitationally stratified, isothermal atmosphere is used. Our focus is on the small structures inside the CS developed in the disrupting magnetic configuration as a result of the catastrophic loss of equilibrium. Some of our efforts are invested in organizing a code with an appropriate distribution of the mesh, so that the numerical diffusion can be suppressed efficiently, the CS could have a reasonably large length, and enough grids could be arranged inside the CS.

In Section 2, we present the initial magnetic configuration, a description of the numerical method, including the code we are using and simulation domain. In Section 3, we describe the mesh refinement strategy and the boundary conditions used in our calculations.

In Section 4, we discuss the results of our experiments. Finally, in Section 5 we summarize this work.

2 NUMERICAL METHOD AND MODEL DESCRIPTIONS

We are investigating in this work the evolution in a two-dimensional disrupting magnetic field that was ever studied analytically by Isenberg et al. (1993), Forbes, Priest & Isenberg (1994) and Mei & Lin (2008). The NIRVANA code (Ziegler 2004, 2005, 2008, 2011) is used, which applies the technique of block-structured adaptive mesh and parallel infrastructure to solve the resistive magnetohydrodynamic (MHD) equations in conservation form:

$$\partial_t \rho + \nabla \cdot (\rho \mathbf{v}) = 0, \quad (1)$$

$$\begin{aligned} \partial_t e + \nabla \cdot \left[\left(e + p + \frac{1}{2\mu_0} |\mathbf{B}|^2 \right) \mathbf{I} - \frac{1}{\mu_0} (\mathbf{v} \cdot \mathbf{B}) \mathbf{B} \right] \\ = \rho \mathbf{g} \cdot \mathbf{v} + \nabla \cdot \left[\frac{\eta}{\mu_0} \mathbf{B} \times (\nabla \times \mathbf{B}) \right], \end{aligned} \quad (2)$$

$$\partial_t (\rho \mathbf{v}) + \nabla \cdot \left[\rho \mathbf{v} \mathbf{v} + \left(p + \frac{1}{2\mu_0} |\mathbf{B}|^2 \right) \mathbf{I} - \frac{1}{\mu_0} \mathbf{B} \mathbf{B} \right] = \rho \mathbf{g}, \quad (3)$$

$$\partial_t \mathbf{B} - \nabla \times (\mathbf{v} \times \mathbf{B}) = -\nabla \times (\eta \nabla \times \mathbf{B}). \quad (4)$$

Here, the conserved variables are the gas density ρ , the momentum $\rho \mathbf{v}$, the total energy e (including magnetic energy, kinetic energy and thermal energy) and the magnetic field \mathbf{B} . The external force $\rho \mathbf{g}$ is the gravity force, μ_0 is the magnetic permeability in vacuum and η is the magnetic diffusivity. The pressure is calculated from the equation of state for an ideal gas, $p = (\gamma - 1)[e - \rho v^2/2 - \mathbf{B}^2/(2\mu_0)]$, assuming that the plasma consists of completely ionized hydrogen, and $\gamma = 5/3$ is the ratio of specific heats. We note here that the focus of the present work is mainly on the kinetic behaviours of the plasmoid and on the detailed fragmentation process of the CS, and the thermal properties of the CS will be studied in the future. Therefore, the radiative cooling mechanism is not considered in the present work.

The above equations are supplemented by the divergence-free constraint for the magnetic field

$$\nabla \cdot \mathbf{B} = 0, \quad (5)$$

which, once satisfied initially, is maintained forever according to the Faraday's law (equation 4). The NIRVANA code adopts a second-order, directionally unsplit central-upwind algorithm of the Godunov-type in conjunction with the constrained transport method to realize the divergence-free condition of the magnetic field.

2.1 The initial configuration

The initial configuration of the magnetic field of interest is based on the work by Isenberg et al. (1993) and Mei & Lin (2008). It consists of an evolutionary sequence of force-free equilibria in response to the quasi-static evolution of the photosphere. This change is slow compared to the traverse of the magneto-acoustic wave across the magnetic configuration. The background field of the configuration is produced by a quadrupole of strength $125\sigma\mu_0 I_0/(96\pi)$ at the depth of d below the photospheric surface, of which the corresponding flux function on the boundary surface reads as

$$A(x, 0) = \frac{125\sigma\mu_0 I_0}{96\pi} \frac{d^2(d^2 - x^2)}{(d^2 + x^2)^2}, \quad (6)$$

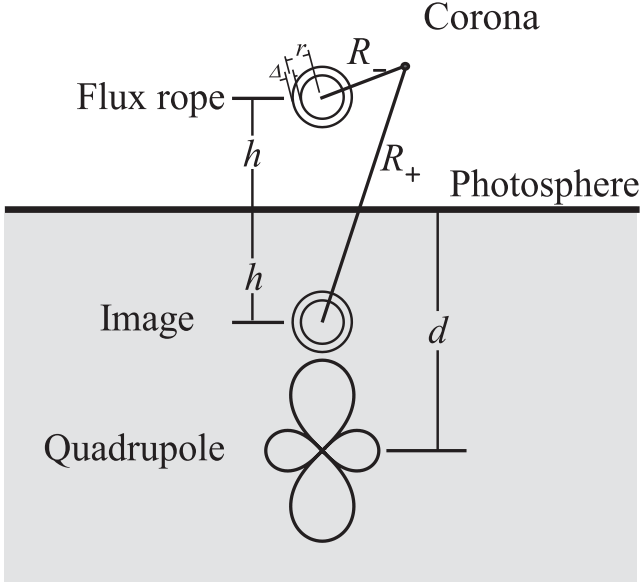


Figure 1. Sketch of the initial magnetic structure, including a flux rope, its mirror image below the photosphere and a buried quadrupole. R_{\pm} , r and Δ are defined later.

where σ is the relative strength of the source and I_0 is a constant in units of the electric current intensity. The corresponding magnetic configuration including the flux rope is governed by

$$iB_x + B_y = \frac{\mu_0 I_0}{4\pi} \left[\frac{4idhJ}{h^2 + \xi^2} - \frac{125d^3\sigma}{16(id + \xi)^3} \right] \quad (7)$$

before the formation of the CS in the framework of the analytic solution, which can be obtained by setting q in equation (31) of Mei & Lin (2008) to zero. The equation that governs the magnetic configuration including a vertical CS attached to the bottom surface is very complicated, and is thus not presented here. The interested readers are referred to Isenberg et al. (1993) and Mei & Lin (2008) for details. Here, $\xi = x + iy$ and J is the intensity of the electric current flowing inside the flux rope in units of I_0 . Fig. 1 shows the sketch of initial magnetic structure described above. In the work of Isenberg et al. (1993), diffusion in the corona is prohibited, and a vertical CS develops with its lower end attached to the bottom surface as the system evolves, pushing the flux rope to move gradually upwards. They noticed that the equilibrium height of the flux rope h depends on σ as shown in Fig. 2.

Fig. 2 shows three typical evolutionary features of the system for different values of r_0 , the initial radius of the flux rope. In the case of small r_0 , say $r_0 = 0.1d$, the quasi-static evolution of the system along the lower level of the equilibrium curve (see the dashed curve in Fig. 2) eventually ends up with a loss of equilibrium as the flux rope reaches its critical height at the turning point on the curve. In the case of large r_0 , for example $r_0 = 0.2d$, the quasi-static evolution of the system continues without end and no loss of equilibrium occurs (see the dotted curve in Fig. 2). A marginal case with $r_0 = 0.15d$ is displayed in the figure for comparison.

The situation in reality is different, however. Resistive diffusion prevents the CS from forming during quasi-static evolution, see discussions of Lin, Forbes & Isenberg (2001). Lin & van Ballegooyen (2002) pointed out that the absence of the CS in a slowly evolving system allows the catastrophe to take place easily, and the above dependence on r_0 does not show. This result allows us to deal with the problem before the system loses the equilibrium via an easy approach in the numerical experiment without worrying about the

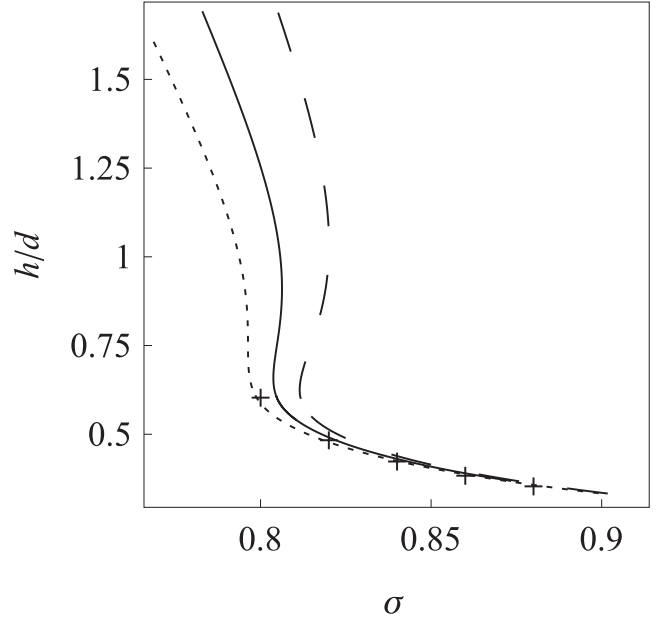


Figure 2. The equilibrium heights of the flux rope h compared to d as a function of the relative strength of the background field σ for different values of the initial radius r_0 of the flux rope: $r_0 = 0.1d$ (dashed curve), $r_0 = 0.15d$ (solid curve) and $r_0 = 0.2d$ (dotted curve).

dependence of the system's catastrophic behaviour on the initial radius of the flux rope. Furthermore, we note here that equation (7) is valid only for the outer region far away from the centre of the flux rope, or for the case that the flux rope is considered an infinitely thin wire. In order to include the electric current distribution in the flux rope, we use the method of Forbes (1990) to rewrite equation (7), so that the current distribution of the flux rope can be incorporated easily.

Following Isenberg et al. (1993), we define a flux rope with finite radius and smooth current distribution that could maintain an approximate internal balance by using the method of Forbes (1990),

$$\begin{aligned} j_z(R_-) &= j_0 J, & 0 \leq R_- < (r - \Delta/2) \\ j_z(R_-) &= j_0 J \{ \cos[\pi(R_- - r + \Delta/2)/\Delta] + 1 \} / 2, & (r - \Delta/2) \leq R_- < (r + \Delta/2) \\ j_z(R_-) &= 0, & R_- \geq (r + \Delta/2), \end{aligned} \quad (8)$$

where $r = 0.125d$, $\Delta = 0.025d$, $R_- = \sqrt{x^2 + (y - h_0)^2}$, j_0 is the maximum current density at the centre of the flux rope, which is related to r , I_0 and Δ in the following way:

$$j_0 = I_0 / [\pi(r^2 + \Delta^2/4 - 2\Delta^2/\pi)]. \quad (9)$$

With such a set-up of the parameters for the flux rope, the initial radius of the rope is $r_0 = r + \Delta = 0.15d$. This arrangement may cause the system in our calculations to evolve along the solid curve shown in Fig. 2 in the quasi-static stage. In the numerical experiment framework, we describe the magnetic field in the following way by considering the electric current distribution in the flux rope and the magnetic field given by equations (7) and (8),

$$\begin{aligned} B_x &= B_\phi(R_-)(y - h_0)/R_- - B_\phi(R_+)(y + h_0)/R_+ \\ &\quad - B_\phi(r + \Delta/2)Md(r + \Delta/2)(d + y) \\ &\quad (3x^2 - (y + d)^2)/R_d^6, \\ B_y &= -B_\phi(R_-)x/R_- + B_\phi(R_+)x/R_+ - B_\phi(r + \Delta/2) \\ &\quad Md(r + \Delta/2)x(-x^2 + 3(d + y)^2)/R_d^6, \end{aligned} \quad (10)$$

where

$$B_\phi(R) = -j_0 J R/2, \quad 0 \leq R < r - \Delta/2 \quad (11)$$

$$\begin{aligned} B_\phi(R) = & -j_0 J \{(r - \Delta/2)^2/2 - (\Delta/\pi)^2 + R^2/2 \\ & + (\Delta R/\pi) \sin[\pi(R - r + \Delta/2)/\Delta] \\ & + (\Delta/\pi)^2 \cos[\pi(R - r + \Delta/2)/\Delta]\}/(2R), \\ & r - \Delta/2 \leq R < r + \Delta/2 \end{aligned} \quad (12)$$

$$B_\phi(R) = -j_0 J [r^2 + (\Delta/2)^2 - 2(\Delta/\pi)^2]/(2R), \quad R \geq r + \Delta/2 \quad (13)$$

and

$$R_+^2 = x^2 + (y + h_0)^2, \quad (14)$$

$$R_d^2 = x^2 + (y + d)^2, \quad (15)$$

$$M = 125\sigma/32. \quad (16)$$

In equation (10), the terms with R_- come from the flux rope and the terms with R_+ originate from its mirror image below the photosphere, and the terms with M are the contribution of the quadrupole.

In addition to the electric current and the magnetic field, the flux rope also includes cold plasma that is believed to come from the chromosphere (e.g. Mackay & van Ballegoijen 2009 and references therein). Therefore, a thin shell surrounding the flux rope exists to separate the hot corona and the cold filament material. In the numerical experiment, in order to avoid apparent numerical diffusion caused by a sharp change on the boundary of the flux rope, we smooth the temperature distribution in the outer shell of the flux rope, also known as the prominence–corona transition region (PCTR), so that the initial temperature distribution inside the flux rope is given by

$$\begin{aligned} T(R_-) &= T_f, \quad 0 \leq R_- < (r - \Delta/2) \\ T(R_-) &= (T_c - T_f)(R_- - r + \Delta/2)/\Delta + T_f, \\ & (r - \Delta/2) \leq R_- < (r + \Delta/2) \\ T(R_-) &= 0, \quad R_- \geq (r + \Delta/2), \end{aligned} \quad (17)$$

where $T_f = 5 \times 10^4$ K and $T_c = 10^6$ K. The internal pressure distribution in the flux rope is given by

$$p_r(y) = p(y) - \int_{R_-}^{\infty} B_\phi(R) j(R) dR, \quad (18)$$

where $p(y)$ is the pressure of the ambient corona.

In this work, the quadrupole source is buried below the photospheric surface at a depth $d = 0.4L_0$ and $j_0 = 1.07 \times 10^{-2}$ A m $^{-2}$. This yields a strength of the magnetic field of about 150 G at the origin. Here, the characteristic length is $L_0 = 10^5$ km. Five groups of parameters, σ , j_0 and J are given in Table 1 according to the works by Isenberg et al. (1993) and Mei & Lin (2008), and the locations of the flux rope corresponding to these combinations of parameters are marked by crosses in Fig. 2. The magnetic structure is in stable equilibrium in the first four cases, and the system could evolve gradually as the parameters in case 1 slowly change into those in case 4. For parameters given for case 5, on the other hand, the configuration is not in equilibrium (see the cross at the extreme left). Therefore, the system cannot evolve from the configuration in the other four cases smoothly to the one in case 5 as a result of the gradual change in the background field. Instead, as the system evolves along the solid curve, the loss of equilibrium would take place at the turning

Table 1. Parameters for magnetic configurations including a flux rope for $r_0 = 0.15d$, and $j_0 = 1.07 \times 10^{-2}$ A m $^{-2}$ for five cases.

Point	h/d	σ	$j_0 J$ (A m $^{-2}$)
1	0.36	0.88	1.05×10^{-2}
2	0.39	0.86	1.038×10^{-2}
3	0.43	0.84	1.028×10^{-2}
4	0.49	0.82	1.017×10^{-2}
5	0.61	0.80	0.974×10^{-2}

point on this curve. In our experiment, we do not evolve the system along this curve because the main goal of the work is to study the fine structure inside the reconnecting CS in the eruption, and we start the experiment directly from the configuration corresponding to case 5 in order to save computational resources.

2.2 Gravitationally stratified solar atmosphere

The domain for our simulations is $-4L_0 \leq x \leq 4L_0$, $0 \leq y \leq 8L_0$, with $y = 0$ representing the base of the photosphere, and the solar atmosphere extending in space of $y > 0$. In order to handle the line-tied boundary condition on the bottom surface, we adopt a multilayer atmosphere structure in our calculations, with $y = h_p$, $y = h_c + h_p$ and $y > h_c + h_p$ representing the top of the photosphere, the top of the chromosphere layer and the extended corona, respectively. The initial temperature distribution is given by

$$\begin{aligned} T(y) &= T_p, \quad 0 \leq y \leq h_p \\ T(y) &= \frac{T_c - T_p}{2} \left\{ \sin \left[\frac{\pi}{h_c} (y - h_p) - \frac{\pi}{2} \right] + 1 \right\} \\ & + T_p, \quad h_p < y \leq h_c + h_p \\ T(y) &= T_c, \quad y > h_c + h_p, \end{aligned} \quad (19)$$

where $T_c = 10^6$ K, $T_p = 5000$ K and $h_p = h_c = 2.5 \times 10^{-3} L_0$. This initial stratified atmosphere is composed of three layers: an isothermal corona with a temperature of T_c , a cooler and denser photospheric layer $y < h_p$ with a temperature of T_p , and a chromosphere that links two regions of different temperatures. The reason why we use such a complex stratified atmosphere is associated with the realization of the boundary condition we shall discuss later. In addition, the gravity $-\rho g$ is in the y -direction and $\mathbf{g} = -g_\odot \hat{y}/(1 + y/R_\odot)^2$ in this set-up. Here, \hat{y} is the unit vector in the y -direction, $g_\odot = 274$ m s $^{-2}$ is the gravitational acceleration near the solar surface and $R_\odot = 6.96 \times 10^8$ m is the solar radius.

Consequently, the gas pressure and the associated density distribution in this atmosphere are given by

$$\begin{aligned} p(y) &= p_p \exp \left[-\frac{y}{1 + y/R_\odot} \frac{m_H g_\odot}{2k_B T_p} \right] \\ & \times \exp \left[\frac{h_p}{1 + h_p/R_\odot} \frac{m_H g_\odot}{2k_B T_p} \right], \quad 0 \leq y \leq h_p \end{aligned} \quad (20)$$

$$p(y) = p_p \exp \left[-\int_{h_p}^y \frac{m_H g_\odot}{2k_B T(y)} \left(1 + \frac{y}{R_\odot} \right)^{-2} dy \right], \quad h_p < y \leq h_c + h_p$$

$$p(y) = p_c \exp \left[-\frac{y h_c}{1 + (y - h_p - h_c)/R_\odot} \frac{m_H g_\odot}{2k_B T_c} \right], \quad y > h_c + h_p$$

$$\rho = \frac{m_H}{2k_B} \frac{p(y)}{T(y)}, \quad (21)$$

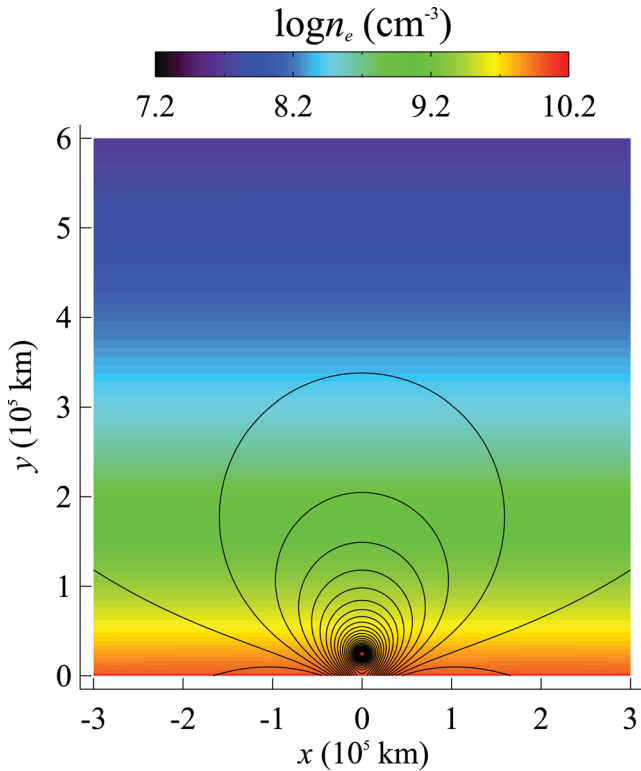


Figure 3. Distributions of the initial magnetic field (black contour lines) and the mass density of an isothermal and gravitationally stratified atmosphere (colour shadings) for $j_0 = 0.01 \text{ A m}^{-2}$ and $p_0 = 0.027 \text{ Pa}$.

where

$$p_p = p_c \exp \left[\int_{h_p}^{h_p+h_c} \frac{m_H g_\odot}{2k_B T(y)} \left(1 + \frac{y}{R_\odot} \right)^{-2} dy \right]. \quad (22)$$

Here, $m_H = 1.67 \times 10^{-27} \text{ kg}$ is the mass of the hydrogen atom, $k_B = 1.38 \times 10^{-23} \text{ erg K}^{-1}$ is the Boltzmann constant, the gas pressure at $y = h_c + h_p$ is $p_c = 0.27 \text{ Pa}$ and the plasma density at $y = h_c + h_p$ is $n_0 = 10^{10} \text{ cm}^{-3}$. With the choice of parameters in this way, the plasma $\beta \approx 3 \times 10^{-4}$ near the flux rope. Fig. 3 shows the magnetic configuration with parameters of case 5, which is not in equilibrium.

3 AMR AND BOUNDARY CONDITION USED IN CALCULATIONS

The adaptive mesh refinement (AMR) in the *NIRVANA* code makes use of the cell-by-cell and the block-structured refinement approaches, in which individual grid cells are divided, and a high adaptivity to solution features could be achieved (Ziegler 2005, 2008). It builds a grid hierarchy composed of generic blocks that have a fixed size of four cells in each coordinate direction. Spatial refinements of the mesh are founded upon hierarchically nested generic blocks where such a nested block has twice the resolution of its parent block. Usually, the calculation grid of *NIRVANA* resembles an oct-tree, including a set of base level (or level 0) blocks that span the whole rectangular computational domain, together with its hierarchy of sub-blocks. The *NIRVANA* code provides two strategies for mesh refinement: one allows users to refine the calculation mesh permanently in any sub-regions and another one allows users to restrict AMR to specified domains during a single run.

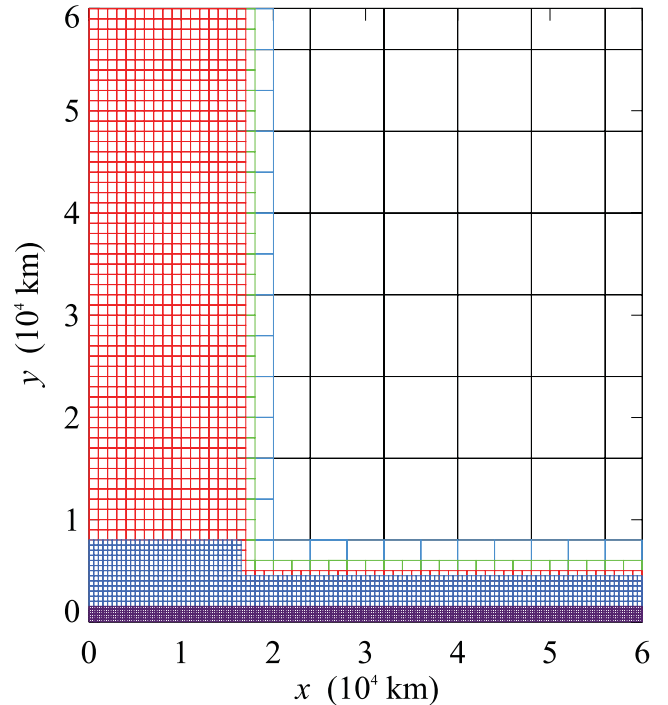


Figure 4. Sketch of the mesh structure used in the present work. Different colours specify steps of the refinement of the grid. The black mesh is of the first level, the blue one is of the second level and the purple one is of the sixth level.

Fig. 4 presents a segment of the calculation mesh used in this work. It utilizes the first strategy to meet the requirement of our problem. Different colours in the figure specify the different refinement levels. In the whole simulation region, the basic calculation grid is arranged in the fashion of 400×400 corresponding to the largest black grid shown in Fig. 4, which yields the largest grid size of $\Delta x = \Delta y = 0.02L_0$. To deal with the large gradient of the plasma density and the gas pressure near the bottom, the level 0 grid in regions of $0.015L_0 < y < 0.05L_0$ and $y < 0.015L_0$ are refined by adding four and five additional refinement levels, respectively, so that the variance of physical quantities in these regions can be resolved well. As can be seen in Fig. 4, the resultant level 4 grid is shown by the blue grid and the level 5 grid by the purple grid, whose sizes are, respectively, $1.25 \times 10^{-3}L_0$ and $6.25 \times 10^{-4}L_0$ in two directions, and are superimposed on the basic grid. In order to improve the resolution in the region close to the flux rope where the magnetic field gradient is large and the plasma β is small compared to those in the other regions, a strip region $|x| < 0.2L_0$ close to the y -axis with three additional refinements is defined. This strip covers the adjacent region of the flux rope from the beginning to the end of the experiment. This is shown in Fig. 4 by the red grid superimposed on the level 0 grid.

The boundary conditions used in this paper are as follows: along the three sides, $x = \pm 4 \times 10^8 \text{ m}$ and $y = 8 \times 10^8 \text{ m}$, we adopt a simple extrapolation method in order to realize an open boundary through which the magnetic field and the plasma can enter or exit the simulation box freely (Forbes & Priest 1984). In general, the simple extrapolation boundary condition may cause small error at the boundary (Orlanski 1976). Especially, the boundary could produce an apparent effect on the system as the moving MHD waves or the magnetic bubble surrounding the flux rope approaches

the boundary. To resolve this problem, we use a larger domain and study the evolution in the system before the magnetic bubble reaches the boundary to reduce the impact of the boundary. This does not increase obviously the burden of computers because the main part of the calculation comes from the vicinity region of the flux rope. At the bottom of the simulation domain, a line-tied boundary condition is used. Because of the low plasma β environment about the bottom boundary, it is a challenge for us to handle the line-tied boundary condition described by Forbes & Priest (1984). As an alternative, we assume very high density in the two thin layers below $y = h_c + h_p$ to approximate the line-tied condition. In this way, we fix all the parameters at the bottom boundary $y = 0$, in order to bypass the complicated behaviour of the plasma and the magnetic field near the bottom boundary due to the low β environment (Yokoyama & Shibata 2001; Nishida et al. 2009). Since we mainly focus on the behaviours of the system in the corona, the line-tied and the frozen flux condition on the bottom boundary is regarded equivalent (see detailed discussion by Forbes 1991).

To this point, we are ready to perform the numerical experiments for the disrupting magnetic configuration following the loss of equilibrium in the system. As indicated earlier, the consequent evolution in the system is governed by equations (1)–(4). During the eruption, the flux rope rises quickly stretching the whole magnetic structure outwards severely, and a CS forms between two magnetic fields of opposite polarity. As the CS becomes longer, it becomes unstable to many plasma instabilities, and the turbulence of various modes commences to develop inside, causing the CS to be fragmented, which invokes fast reconnection through the CS. Therefore, the reconnecting CS includes many small and fine structures. To help resolve and identify these small features, we introduce further AMR in the region where the CS forms and develops. This region is a strip defined as

$$|x|/L_0 \leq 3 \times 10^{-3}, \\ 3 \times 10^{-3} \leq y/L_0 \leq 0.1 + 8 \times 10^{-4}(t - 120). \quad (23)$$

Each value appearing in equation (23) is determined via a series of adjustment by running the code several times until the strip region is able to include the whole sheet in the experiment. The value 120 is chosen because the sheet begins to appear and grow at $t = 120$ s, from which the strip is also embedded in the code to help resolve the sheet. Up to seven additional levels of mesh refinement are inserted, and the size of the minimum grid in both x - and y -directions is $1.5625 \times 10^{-4}L_0$ in this strip region.

We set a uniform physical magnetic diffusivity $\eta = 5 \times 10^8 \text{ m}^2 \text{ s}^{-1}$ in this strip at the beginning, and simply set the physical diffusion to be zero outside. Before experiments commence, it is necessary to roughly estimate the numerical diffusion compared to the physical one. Rewriting equation (4) gives

$$\partial_t \mathbf{A} - \mathbf{v} \times \mathbf{B} + \eta \nabla \times \mathbf{B} = 0, \quad (24)$$

which holds exactly in the absence of the numerical diffusion. In any numerical experiment, on the other hand, the numerical diffusion is inevitable. Thus, the above equation does hold unless an extra diffusive term, η_n , is included, such that

$$\partial_t \mathbf{A} - \mathbf{v} \times \mathbf{B} + (\eta - \eta_n) \nabla \times \mathbf{B} = 0, \quad (25)$$

where η_n is the numerical diffusivity.

Fig. 5 plots the averaged ratio η_n/η in the strip mentioned above versus t in the period of $200 < t < 700$ s. According to the plot, the numerical diffusion ranges from 10 to 20 per cent of the physical diffusion on average, and exhibits an oscillating feature which might be related to the generation of the magnetic island in the CS (see

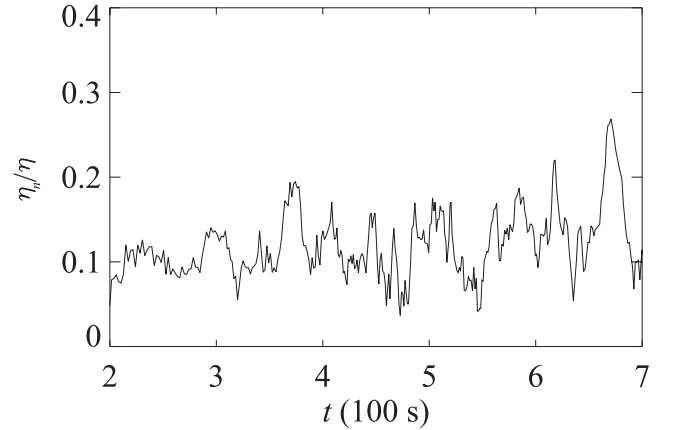


Figure 5. Ratio of the numerical resistivity η_n to the physical one η versus time.

detailed discussions later). Comparing with that shown by Shen et al. (2011), the overall numerical diffusion in this work is apparently depressed. Therefore, the impact of the numerical diffusion on the experiment results can be reasonably ignored.

4 RESULTS OF NUMERICAL EXPERIMENTS

Before studying the reconnection process in CS during the eruption, we perform a set of tests to check whether the state governed by the lower branch of the solid curve in Fig. 2 could be realized in the system investigated here since those states shown in Fig. 2 were from an analytic solution. Five points were selected as marked in Fig. 2, with the corresponding parameters listed in Table 1, and for a specific case, the system starts to evolve from the state governed by the corresponding parameter combination. As expected, the flux rope in the first four cases oscillates at the beginning and eventually finds its equilibrium positions quickly, which are not on the solid curve in Fig. 2, but are somewhere very close. The deviation obviously results from the difference between the way of describing the system analytically and numerically. Here, damping of the oscillation is due to the numerical dissipation since the physical one has not been introduced yet. In case 5, as expected, the flux rope is not in equilibrium, and it starts moving upward at the very beginning in an apparent acceleration fashion.

4.1 Evolution in the global configuration

Since the evolution starts in a non-equilibrium state, the flux rope commences to rise with an acceleration of about 0.1 km s^{-2} at the very beginning of the experiment. Snapshots of the overall magnetic structure in the evolution and the relevant density distribution of the plasma in the system are shown in Fig. 6. A fast-mode shock is seen to appear in front of the flux rope at a height of $h = 0.5L_0$ when $t = 30$ s, at which the speed of the plasma driven by the motion of the flux rope exceeds the local fast magneto-acoustic speed. The fast shock propagates outward and forms a crescent-shaped front separating disturbed and undisturbed plasmas from one another. Fast expansion of the disrupting magnetic field results in the lower density in the disturbed region than in the undisturbed region. Near the shock front, the plasma undergoes adiabatic compression and increases the density and temperature in the nearby area.

A CS starts to form behind the flux rope at $t = 120$ s as a result of severe stretching of the magnetic field by the eruption (see also discussions of Isenberg et al. 1993; Lin & Forbes 2000). Magnetic

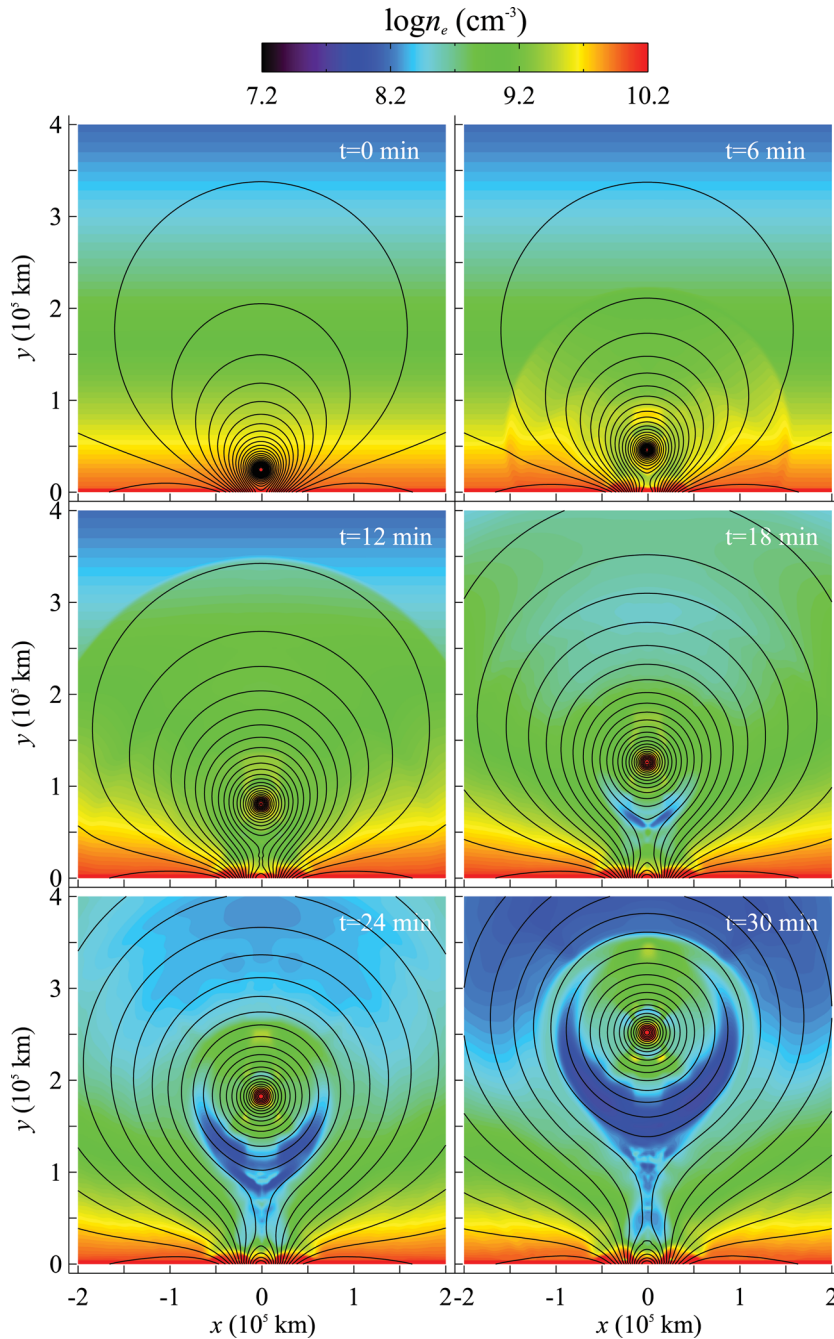


Figure 6. Snapshots of the magnetic field (black contour lines) and the coronal mass density (colour shadings) at six time instances of the eruption.

reconnection in the CS converts magnetic energy to thermal and kinetic energy, the plasma in the reconnection outflow is heated to high temperature and squeezed out of CS as shown in Fig. 7 (see those arrows in the CS). The outflow moving upward eventually enters the CME bubble around the flux rope along the separatrix through the upper tip of CS and forms a hot shell enveloping the CME as suggested by both observations (Raymond et al. 2003) and the theory (Lin, Raymond & van Ballegoijen 2004; Lin & Soon 2004). The shell, the flux rope and the region between them constitute the so-called three components of CMEs. The shell appears at around $t = 12$ min and disappears eventually at $t = 30$ min. According to the plots shown in Fig. 6 at $t = 30$ min, the density is about $5 \times 10^7 \text{ cm}^{-3}$ in the vicinity of CS and in the shell surrounding the

CME compared to that of about 10^{10} cm^{-3} at $t = 12$ min in the same structures. The corresponding temperature distribution is given in Fig. 7, which indicates that the plasma in the CS and at the bottom of the CME bubble is heated to very high temperature (up to a few times 10^7 K), but it is important to note that radiative cooling is not included in the computations.

In addition to the hot shell surrounding the flux rope, another region with lower temperature behind the fast shock can be seen clearly after $t = 18$ min, and it is co-located with the dimming region in space. Compared with the high temperature in the shell, this region is a low-temperature region with the lowest value of 10^5 K . In the early stage of an experiment ($t < 12$ min), the velocity of the flux rope is less than 100 km s^{-1} , which is so slow that it cannot maintain

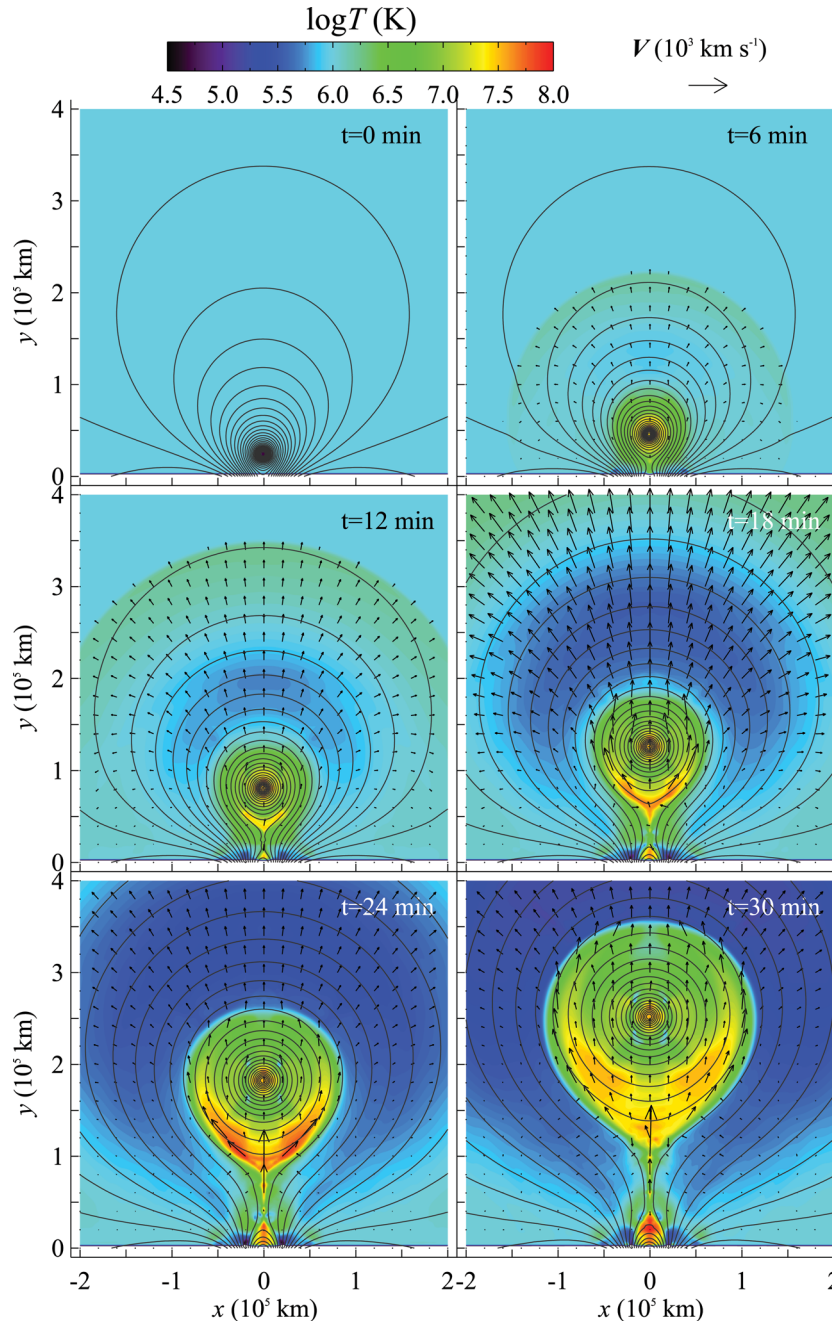


Figure 7. Snapshots for the temperature (colour shadings) and the plasma flow at six time instances of the eruption.

sharp changes in the density and the temperature between the fast shock and the dimming region because the plasma has enough time to adjust the density and temperature distributions. Later on, the flux rope rises at a velocity of about 200 km s^{-1} and the plasma in the fast shock is driven to a velocity exceeding 600 km s^{-1} . This quick flow produces a dimming region following the shock front and leaves no time for the plasma in the vicinity to refill it. Thus, the plasma in the dimming region undergoes an adiabatic expansion that accounts for both the low-density and the low-temperature features there.

As indicated in Figs 6 and Fig. 7, the formation and the development of the CS behind the flux rope are associated with the motion of the flux rope. We see from these two figures the Y-point structure at both the lower tip (p) and the upper tip (q) of the CS. Fig. 8(a) gives

an example of the magnetic structure at $t = 520 \text{ s}$ with the height of the flux rope (h), p and q denoted. Magnetic field lines attached to q and p of the CS are the separatrices represented by the dashed curves, which compose the outer shell of the CME bubble and the outermost layer of the flare loop system, respectively. Here we follow previous practice for analytic solutions, and use an infinitely thin line to represent the CS with its lower tip at $y = p$ and upper tip at $y = q$. The height of the flux rope at this time is $y = h$. The Y-point appears at both the tips of the CS as a result of the approximate force-free and low β environment. Variations of h , q and p versus t , and the corresponding velocities are plotted in Figs 8(b) and (c), respectively. During the whole period we perform the experiment, the motion of the flux rope has a constant acceleration of 0.1 km s^{-2} .

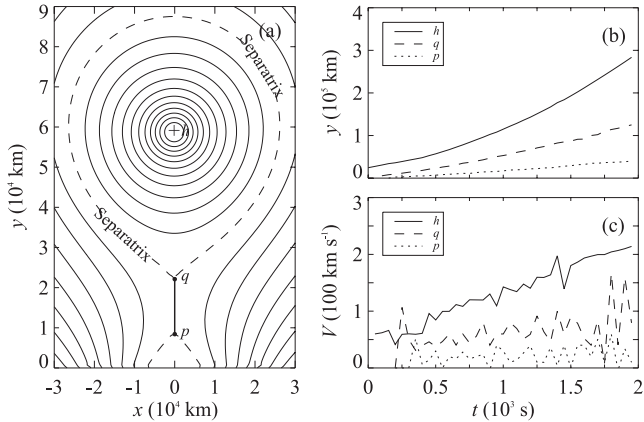


Figure 8. (a) Magnetic configuration in the eruption at $t = 520$ s, in which the magnetic separatrices are plotted by the dashed curve. The centre of the flux rope at height h is indicated by '+', and the upper and the lower tips of the CS are marked by q and p , respectively. (b) Heights of the flux rope (solid line), the upper tip of the CS (dashed line) and the lower tip of the CS (dotted line) versus time; and (c) velocities of h , q and p versus time.

The velocity of flux rope increases from about 50 km s^{-1} at $t = 4$ min to 220 km s^{-1} at $t = 32$ min. Meanwhile, the average velocity of q is about 50 km s^{-1} with an acceleration of 36 m s^{-2} ; the velocity of p moves roughly constantly at about 15 km s^{-1} without showing apparent acceleration. This results in the extension of CS in length at a speed of about 35 km s^{-1} . The speed of the lower top of the CS, p , is similar to that deduced theoretically (see Lin 2002), but the motion of q shows apparent difference with the theoretical results. This is consistent with the result of Lin (2002) such that the motion of p is basically determined by reconnection in the CS and the motion of q depends on the motion of the flux rope in addition. For a comparison with observations, Vršnak, Sudar & Ruždjak (2005) presented a statistical analysis of 545 flare-associated CMEs and 104 non-flare CMEs observed in the heliocentric distance ranging from 2 to 30 solar radii, and found that velocities of CMEs at 3 solar radii are in the range from 150 to 10^3 km s^{-1} with the most possible value of 400 km s^{-1} , and accelerations of CMEs range from -0.03 to 0.03 km s^{-2} .

4.2 Sweet–Parker reconnection stage

As indicated in Figs 8(b) and (c), the CS is a process of dynamical evolution. Therefore, various plasma instabilities and the resultant turbulence are expected to develop in the CS. According to the features appearing in CS during the eruption, the evolution in the CS consists of four stages: (1) the loss of the equilibrium in the system occurs, and the CS does not appear yet; (2) the CS forms and extends in the length, and manifests a fashion of the Sweet–Parker reconnection; (3) fragmentation of the CS occurs; and (4) magnetic islands or plasma blobs continue to form, and the CS evolves to a Petschek-type configuration in large scale.

In the first stage ($t \leq 120$ s), the flux rope loses the equilibrium and commences to move upward. Due to the existence of numerical diffusion, no CS appears, but a distorted X point forms below the flux rope at the very beginning. After the velocity of the flux rope exceeds 30 km s^{-1} at $t = 120$ s, the X point evolves into a CS that grows continuously. Meanwhile, the AMR technique starts to work in the vicinity of CS as indicated by equation (23), which reduces the numerical diffusion further and allows the CS and the energy

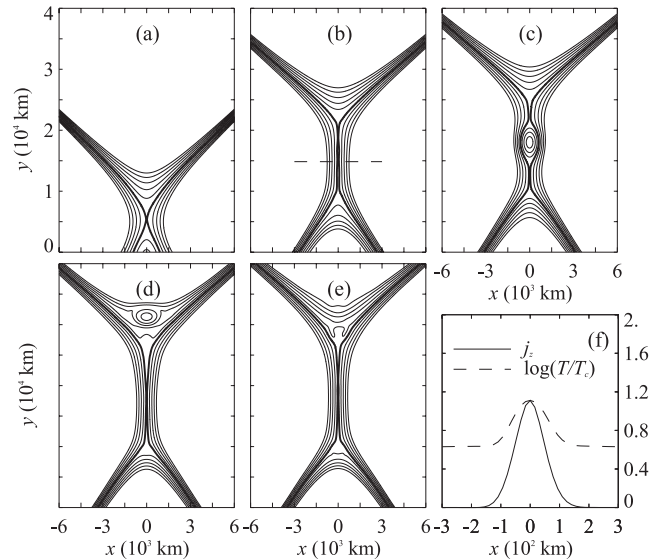


Figure 9. (a–e) The magnetic field configurations near the X point or the CS (thick lines) at $t = 115, 255, 290, 309$ and 320 s, respectively. (f) Distributions of the normalized j_z and $\log(T/T_c)$ along the horizontal dashed line $y = 0.075L_0$ shown in (b).

conversion inside CS to develop at a rate consistent with the adopted resistivity.

The second stage ($120 < t < 255$ s) starts with the appearance of the CS and ends with the onset of the tearing mode instability. During this period, the length of CS increases from 0 to $0.11L_0$ without producing any magnetic islands as shown in Figs 9(a) and (b). The first magnetic island or plasma blob forms at $t = 255$ s (Fig. 9c), which indicates the initiation of the tearing mode. Figs 9(d) and (e) give the magnetic field configurations near the CS (thick lines) during this stage. Fig. 9(f) presents distributions of $|j_z|$ and $\log(T/T_c)$, respectively, along the horizontal dashed line at $y = 0.075L_0$ as shown in Fig. 9(b). According to the j_z profile, we are able to determine the thickness of the CS, which is $\delta_{CS} \approx 200 \text{ km}$, and the length of the CS at the same time can be determined by the plot in Fig. 9(b), which is $L_{CS} = 1.1 \times 10^4 \text{ km}$. Therefore, we find the CS aspect ratio $L_{CS}/\delta_{CS} \approx 55$ at $t = 255$ s right before the formation of the first magnetic island inside the CS. This result is important for improving our knowledge of the tearing mode instability in the reconnecting CS that evolves in the dynamic process.

In the framework of the linear theory for the tearing mode (e.g. see Furth, Killeen & Rosenbluth 1963), the sheet becomes unstable to the tearing mode as the aspect ratio exceeds 2π . The non-linear investigation on the reconnecting CS found that, on the other hand, the CS could remain stable even as the aspect ratio exceeds 50. For example, Loureiro et al. (2007) noticed that the CS becomes torn as the ratio reached up to 60, and Ni et al. (2010) even found that the tearing mode did not commence until the ratio was close to 100. Furthermore, Shen et al. (2011) realized that it takes a while for the tearing mode to develop even though the CS is very long. Therefore, the reconnection process needs to undergo a gradual stage, namely the Sweet–Parker reconnection stage, in the configuration evolving from the equilibrium state, before fast evolution commences due to instabilities occurring in the CS. As compared to these existing results, what is new and interesting about our results revealed in Fig. 9 is that they are obtained for the CS in a dynamic process, and both the length and the thickness of the CS change in a dynamic fashion. Thus, for resistive MHD, we conclude that magnetic reconnection

in CS should always go through a slow stage no matter whether the CS configuration is initially in equilibrium or in a fast developing process.

Following its appearance at $t = 255$ s, i.e. 125 s after the formation of the CS, the first plasmoid quickly moves upward at a speed of around 800 km s^{-1} , which is roughly the local Alfvén speed near the site it starts to form. At $t = 320$ s, it leaves the CS through the CS upper tip and collides with the bottom of the closed magnetic field surrounding the flux rope. The second plasmoid appears at $t = 324$ s, and moves downward, about 69 s after the first one. The third plasmoid starts to form at $t = 345$ s, and moves upward about 21 s after the second one. Within the following 30 min, up to 150 plasmoids are observed to appear successively. Qualitatively, the time intervals we deduced here between the first plasmoid and the subsequent ones are consistent with that estimated by Shibata & Tanuma (2001). Quantitatively, Shibata & Tanuma (2001) suggested that it takes up to 10^6 s for the first plasmoid to form, and the second one appears 10^3 s after the first one. The difference between the two works is because the resistivity used in this work ($5 \times 10^8 \text{ m}^2 \text{ s}^{-1}$) is much larger than that used by Shibata & Tanuma (2001), which is $10^4 \text{ cm}^2 \text{ s}^{-1}$. If we duplicate their estimate with $\eta = 5 \times 10^8 \text{ m}^2 \text{ s}^{-1}$, we end up with roughly the same results as we have above. Thus, our results support the conclusions of Shibata & Tanuma (2001).

4.3 Stage of the fractal and Petschek-type reconnection

Fig. 10 displays a snapshot of the distribution of three parameters around the CS at $t = 13.9$ min. These parameters are plasma density (Fig. 10a), velocity (Fig. 10b) and electric current (Fig. 10c). At this time, q , p and the length of CS ($q - p$) are about $0.15L_0$, $0.42L_0$ and $0.27L_0$, respectively, and the location of the principle X point (PX point) is indicated in Fig. 10(b). Region $R1$ surrounded by a rectangle in Fig. 10(b) and some parameters therein will be measured

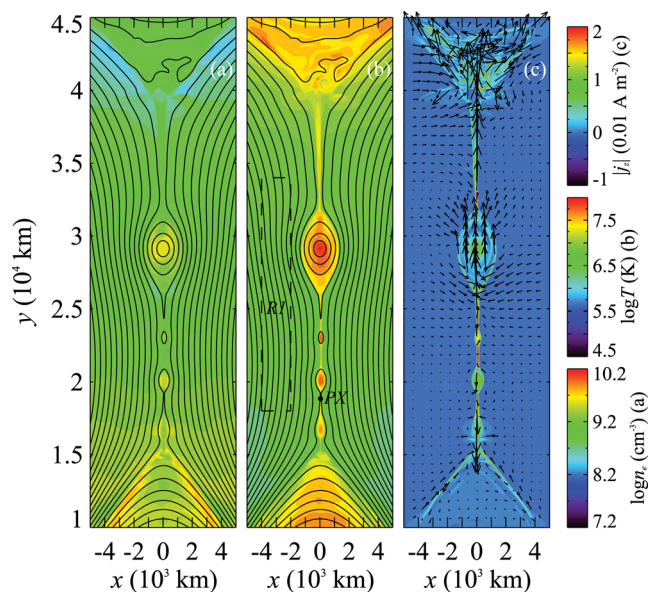


Figure 10. A snapshot of distributions of various parameters in a region including the CS at $t = 13.9$ min. The continuous contours in black in each panel are for the magnetic field, the colour shadings are for the density (a), the temperature (b) and the electric current (c), respectively. Those arrows in (c) specify the plasma flow, the PX point is marked in (b). A rectangle region $R1$ is selected in (b) as well, and some parameters in it will be measured and discussed later.

and discussed later. The most remarkable feature in these panels is those four plasmoids of different sizes dividing the CS into several pieces. In one piece between two adjacent plasmoids right below the largest one, the CS is more like a Sweet–Parker configuration with a thickness of about 200 km. However, the piece upon the largest plasmoid shows a bifurcating structure that looks like the Petschek slow-mode shock, and it can be seen clearly in the experiment that both the magnetic field and the plasma are apparently disturbed as the plasmoid goes through this region. Due to interactions between the reconnection outflow and the plasmoids, an intense turbulent region occurs near the upper tip of the CS. As shown in Fig. 10(c), distribution of the electric current in this region manifests many fine structures and fairly complex flow patterns. The turbulence in this region dissipates most of the magnetic energy and part of kinetic energy of the plasmoid to allow the plasmoid to merge into the CME bubble. As Lin et al. (2004) and Lin & Soon (2004) noticed, much (at least half) of the mass and the magnetic flux observed in CME are brought by reconnection from the corona into the CS and then into the CME bubble. Obviously, our numerical experiment reveals more details of the process in which the reconnected plasma and magnetic flux enter the CME bubble.

With continuous rising of the flux rope, the CS is stretched further, and more and more magnetic islands appear in the CS. We noticed that the magnetic field and plasma structures between two adjacent islands or plasmoids manifest the Petschek-type features (Petschek 1964). To demonstrate this, we plot the distribution of the electric current density in Fig. 11(a), in the region of $-0.4L_0 < x < 0.4L_0$ and $0.3L_0 < y < 1.05L_0$ at $t = 29$ min. Several plasmoids in the CS are easily recognized, and turbulent patterns on the top of the flare loop and below the bottom of the CME bubble can also be seen. At this stage, the speed of the CS extension in length is about 35 km s^{-1} as indicated in Fig. 8(c).

Similar to the experiments by Shen et al. (2011), the bifurcation of plasma flows near the fluid stagnation point (S point) and PX point are also observed in the experiments performed here. To look into more details of the turbulent CS, we select two subregions (surrounded by the dashed-line boxes) in the vicinity of the CS shown in Fig. 11(a), one subregion includes both the S and PX points, and another one is located above the first one. Fig. 11(b) plots the magnetic field (contours) and the plasma flow (arrows) in the first subregion with the S and PX points being marked. As expected, the magnetic field and the plasma flow display an apparent Petschek-type configuration with two pairs of the slow-mode shock separating the reconnection inflow and the outflow from one another (see the contours connecting the S and PX points). The region within the upper pair of the slow-mode shocks is divided into several segments by plasmoids, and several X and O points appear in this region. The lower pair of shocks, on the other hand, are similar to those shown by Forbes (1988), Forbes & Isenberg (1991) and Shen et al. (2011). Because of the dynamic process in the turbulent region, there is not a very clear feature of the stationary termination shock and the deflected shocks suggested by Forbes (1988), but lots of filamentary structures dramatically changing continuously. This is obviously due to the successive interaction between the reconnection outflow and the closed magnetic field below the CS. The fact that experiments by Forbes (1988) did not manifest these numerous fine structures is probably because the resolution of the grid used at that time was not high enough.

Fig. 11(c) displays the distribution of the magnetic field and the plasma flow in another subregion, which is the uppermost segment of the CS, and manifests clearer Petschek-type reconnection than the first one. The distributions of several important parameters along

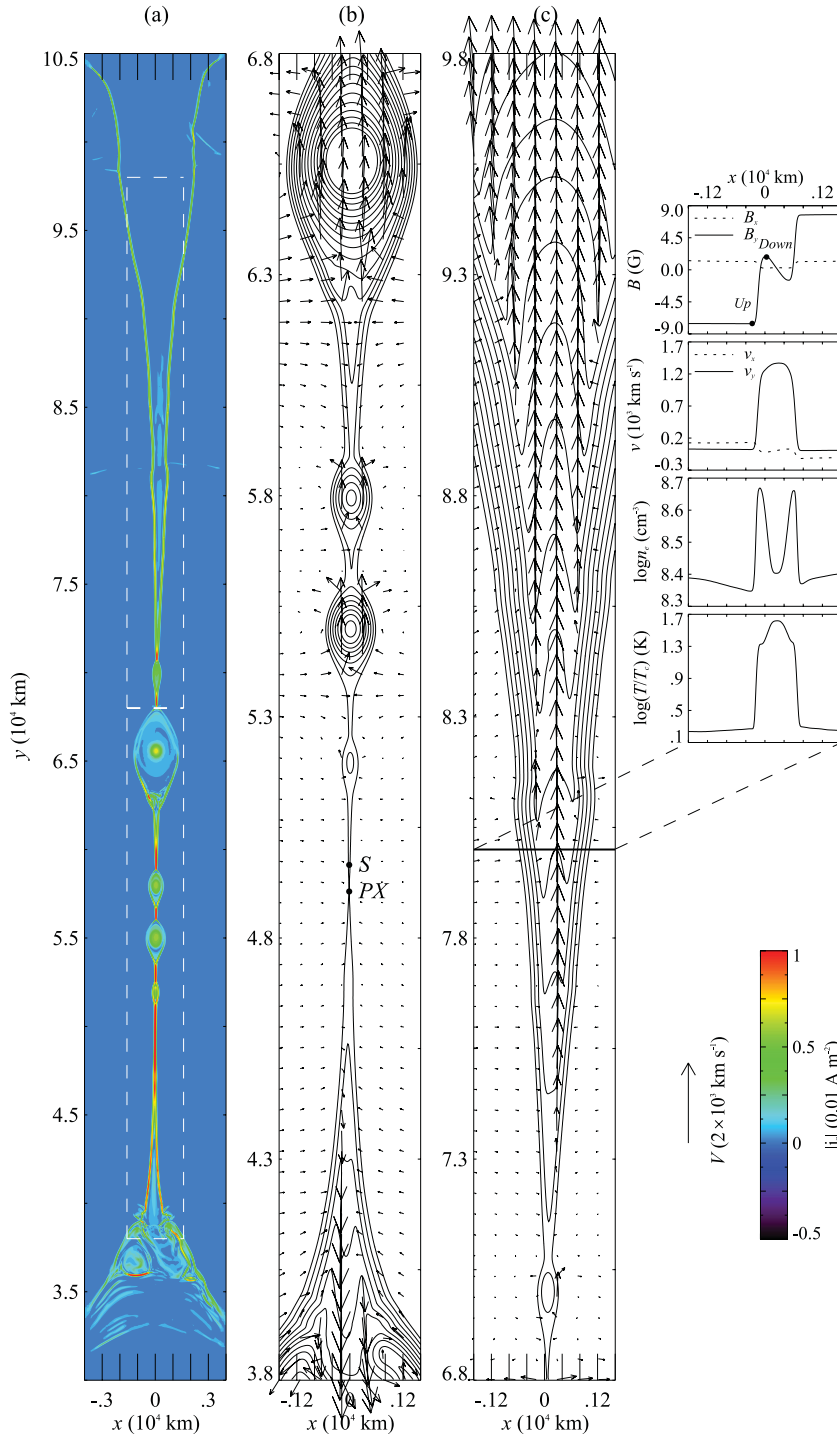


Figure 11. Detailed features of various parameters around the CS seen at $t = 29$ min. Distribution of the electric current is shown in (a), and two smaller rectangular regions surrounded by dashed lines are specified for studying the other parameters in more details. The lower region (b) includes several magnetic islands, the post-flare loop system, as well as the S and PX points, which manifests a scenario of the turbulent reconnection; the upper region (c) displays two slow-mode shocks at either side of the outflow region, and shows typical features of the Petschek-type reconnection. The distributions of parameters along a cut marked on (c) are shown by an inset at the upper right-hand corner.

a cut marked on it (see the horizontal solid line) are shown by an inset at the upper right-hand corner of Fig. 11. As shown in this inset, it is evident that each variable undergoes a stepwise change in a narrow zone between points ‘Up’ and ‘Down’ marked in the plot for B_y . Correspondingly, B_x decreases from 9 G in the upstream to 1 G in the downstream, v_x increases from almost zero to $1.2 \times$

10^3 km s^{-1} , the electron density increases by about two times and the temperature by about 23 times. Sato (1979) and Ugai & Tsuda (1979) had investigated this kind of discontinuous structure in detail, and confirmed it as the slow-mode shock.

Here, in turn, the angle between the shocks is not considered small. A rough estimate according to the magnetic field and the

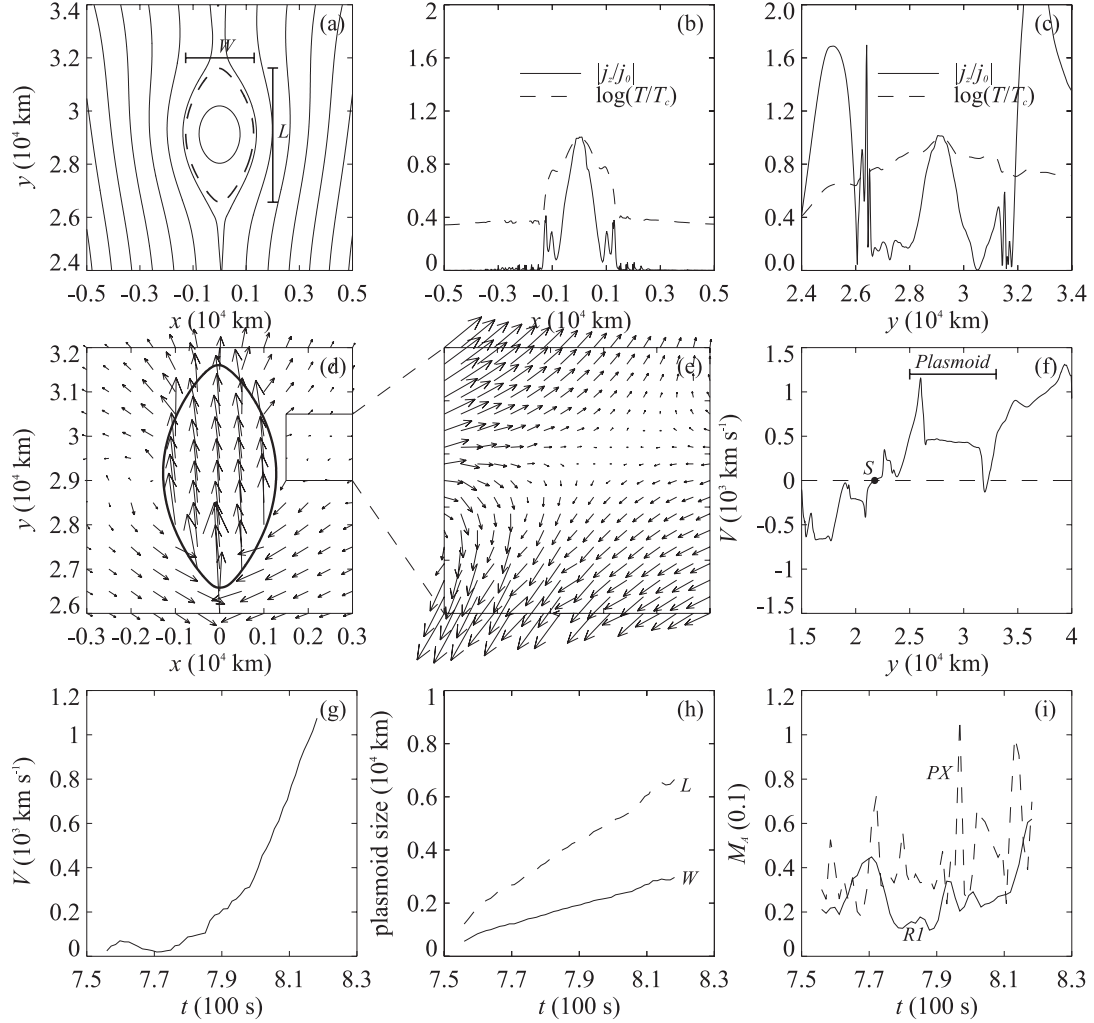


Figure 12. Detailed analyses for the biggest plasmoid shown in Fig. 9. (a) Magnetic lines in the vicinity of plasmoid, whose boundary is highlighted by dashed line. Letters ‘W’ and ‘L’ mark the size of the plasmoid. (b and c) The distribution of normalized $|j_z|$ (solid line) and $\log T/T_c$ (dashed line) along the horizontal line through the centre of the plasmoid and along the y-axis, respectively. (d and e) Distributions of plasma velocity in the local region of the plasmoid and an enlarged local region for the flow field in the box marked in (d). (f) The distribution of the y-component of the plasma velocity along the y-axis (solid line). The dashed line $v_y(0, y) = 0$ is zero-velocity line, and its intersection with the solid line represents the S point. (g) The change in the velocity of the plasmoid versus time t . (h) The changes in W (solid line) and in L (dashed line) versus t . (i) The change in values of M_A at the PX point (solid line), and in regions R1 (dashed line) marked in Fig. 9(b) versus t .

plasma structure shown in Fig. 11(c) brings the angle to the range from 6.5 to 14° . This is different from the expectation based on the standard theory of the Petschek-type reconnection (e.g. see Priest & Forbes 2000, p. 391 for more discussions). The difference seems to result from the formation of the plasmoid in the reconnecting CS, and the standard theory of the Petschek-type reconnection does not include such a scenario. In addition to the plasmoid, the turbulence may also cause the CS to expand in thickness. Considering the known results of theory, observation and numerical experiment so far (e.g. see Petschek 1964; Forbes & Malherbe 1991; Shibata & Tanuma 2001; Ko et al. 2003; Lin et al. 2005, 2007; Bárta et al. 2011; Shen et al. 2011), we realize that the CME/flare CS may not be of a simple shape, but of complex configuration that includes Petschek-type slow shocks, turbulent eddies of various sizes, as well as interactions among these structures.

4.4 Structures and kinematics of plasmoids

As shown in Fig. 10, the temperature inside the plasmoid is higher than the ambient corona, and a typical plasmoid has a two-

component structure as indicated by the distribution of the electric current: a thin shell and a core. However, the plasma density does not display apparent difference from the ambient atmosphere. Taking the largest plasmoid shown in Fig. 10 as an example, a detailed analysis is conducted to look into its physical properties.

Fig. 12 plots various parameters for its geometric scale and physical features. Fig. 12(a) gives the magnetic field lines inside and outside the plasmoid. The separatrix (dashed line) defines the boundary of the plasmoid. The length (‘L’) and the width (‘W’) of the plasmoid as marked in this panel are 5.2×10^3 and 2.6×10^3 km, respectively. Distributions of $|j_z/j_0|$ (solid line) and $\log(T/T_c)$ (dashed line) in the horizontal and vertical directions through the centre of the plasmoid are shown in Figs 12(b) and (c), respectively, as well. The current distribution in Fig. 12(b) shows an apparent two-component structure in the plasmoid, and that in Fig. 12(c) manifests more complex features. Consistent with the shading contour for the electric current in Fig. 11(a), the plasmoid is surrounded by a thin shell with a medium enhancement in the electric current, and inside the shell is a core with stronger current. Such a two-component structure in

the plasmoid is noticed for the first time. Because the density distribution does not show similar feature and there is not an existing method and/or technique available to observe the electric current in the corona, it is not easy to confirm this kind of structure in reality for the time being.

Three peaks are seen in the distribution of the electric current in the vertical direction (see Fig. 12c). Obviously, the peak at the centre is for the plasmoid, and the other two should indicate the CS. We also note that the peak at the centre is lower than the others, suggesting that the current in the plasmoid is weaker than that in the CS. In addition to these peaks, the current intensity near the two ends of the CS at $y = 0.265L_0$ and $0.31L_0$ reveals violent oscillating behaviour, which implies the turbulent structure of the plasma in these areas.

As indicated by the dashed lines in Figs 12(b) and (c), the temperature inside the plasmoid is higher than the CS and the nearby corona. Because of the absence of the cooling mechanisms in the experiments performed here, the average temperature is higher than observed for plasmoids reported by some authors (e.g. see Ohyama & Shibata 1997, 1998; McKenzie & Hudson 1999; McKenzie 2000). On the other hand, according to the snapshots shown in Fig. 7, the temperature of the whole system decreases with time as a result of the adiabatic expansion. Therefore, the temperature of the hottest part inside the flux rope decreases to about 25 MK, and that in the CS decreases to about 15 MK at around $t = 13.9$ min when Figs 10 and 12 are plotted. Here, we note that the highest temperature of the CME bubble around the flux rope could be higher than the temperature of the CS, which is different from expected. This is probably due to the fact that the reconnection outflow continuously brings the plasma heated by reconnection out of the CS, and sends it into the outer shell of the CME. As mentioned earlier, further diffusion occurs in this process as a result of the interaction between the magnetized plasma in the plasmoid with that pre-existing in the CME shell, and it could be partly responsible for increasing the temperature in the CME shell. In contrast, no heated plasma could accumulate inside the CS, and the plasma temperature in the sheet is mainly governed by the strength of the reconnecting magnetic field. As reconnection proceeds, the magnetic field in the upstream region becomes weaker so that the thermal energy released decreases and the temperature in the CS becomes lower. Obviously, such a qualitative and tentative explanation needs further confirmation in the future.

Figs 10(c), 12(d) and 12(e) plot the velocity field of the plasma around the plasmoid. Here, Fig. 12(e) is an enlarged local region surrounded by the square box shown in Fig. 12(d), in which the plasmoid itself is marked by an oval. An obvious discontinuity exists between the interior and the exterior of the plasmoid in the velocity field (Fig. 12d). The plasma inside this plasmoid has an almost uniform velocity field that means that the plasma inside moves upward as a whole. Outside the plasmoid, the motion of the plasmoid drives the plasma in front of it upward, depletes the region below and results in local plasma moving towards the CS behind it (see the flow pattern in Fig. 12e). Interactions among plasma flows in this region result in complex flow structures and an S point near the plasmoid. Therefore, there are two types of turbulence present inside and around the CS. One is due to the plasma instabilities and another one is caused by the motions of the plasmoid and plasma flows. Such two types of turbulence have been studied recently on a kinetic scale by Karlický, Bárta & Nickeler (2012). This result is very important for us to understand how the plasmoid governs the scale, especially the thickness, of the CS.

Previous works by Bárta et al. (2008) and Shen, Lin & Murphy (2011 and references therein) confirmed the contribution of the turbulence invoked by the plasma instabilities to broadening the CS, and detailed studies with higher grid resolution in this work revealed the information on the occurrence of secondary turbulence around and inside the CS (see also fig. 4 of Shen, Lin & Murphy 2011), which may cause further broadening of the CS. This implies that it is not very difficult for the CME/flare CS to possess an extraordinary thickness that is much larger than that expected from the traditional theory of reconnection on the basis of the classical *Spitzer* and anomalous resistivities (see also the discussion of Lin et al. 2007).

In addition, we investigate the other properties of the plasma flow along the y -axis as well. Fig. 12(f) presents the y -component of the plasma velocity $v_y(0, y)$ along the y -axis at $t = 13.9$ min (see also Fig. 10c). The horizontal dashed line indicates the zero velocity, and the intersection of the $v_y(0, y)$ curve with this zero-velocity line determines the location of the S point. We note the existence of an apparent plateau in the $v_y(0, y)$ curve, which indicates again that the matter inside the plasmoid moves upward as a whole. We also see two peaks on the $v_y(0, y)$ curve below and above the plateau: the below peak indicates that the plasma flow after the plasmoid moves faster than the plasmoid, and pushes the latter to move upward, and another peak shows that the plasma in front of the plasmoid moves slower than the plasmoid, preventing the latter from moving upward. This phenomenon has been reported by Shen et al. (2011), which suggests the role of the reconnecting outflow in governing the kinematic features of the plasmoid or the magnetic island inside the fragmented CS. The plasmoid was produced near the S point at about $y = 0.17L_0$, and took around 65 s to travel from the S point to the upper boundary of the CS with an average speed of roughly 10^3 km s⁻¹, and an average acceleration of about 15 km s⁻² (Fig. 12g gives the velocity measured at the plasmoid centre as a function of t).

Fig. 12(h) displays the change in the width (W , solid line) and the length (L , dashed line) of the plasmoid with time t . When the plasmoid moves upward, its size grows with a fixed aspect ratio of about 2. The main contribution to the growth of the plasmoid comes partly from the reconnected plasma and magnetic flux in the reconnection inflow, and partly from the expansion of the plasmoid itself as entering the area of weaker magnetic field outside the CS.

We also study the rate of magnetic reconnection, M_A , the speed of the reconnection inflow compared to the local Alfvén speed v_A near the CS. The value of M_A at different times near the PX point as marked in Fig. 10(b) is shown by the dashed line in Fig. 12(i). On average, it is higher than 0.03 with a couple of peaks appearing close to 0.1. Occurrence of these peaks should somehow be related to the formation of plasmoids in the CS. As a comparison, we estimate M_A in a region R1 as labelled in Fig. 10(b), and the average value of M_A in this box is plotted by the solid line in Fig. 12(i). Apparently, M_A measured near the PX point is higher than that measured in box R1. As expected, the M_A at the PX point has larger value than the outer region of the CS (see also discussions of Lin, Cranmer & Farrugia 2008; Shen et al. 2011).

More information of the plasmoid motion could be revealed by tracking individual plasmoids inside the CS. Following the practice of Shen et al. (2011), we identified a group of plasmoids in the CS, and plot their location along the sheet versus time in Fig. 13(a). Unlike the CS in the case of Shen et al. (2011) that extends over the entire domain, the CS in the present case possesses an upper tip right below the CME bubble. Therefore, the upward motion of the plasmoid stops near the bottom of the bubble as it should happen

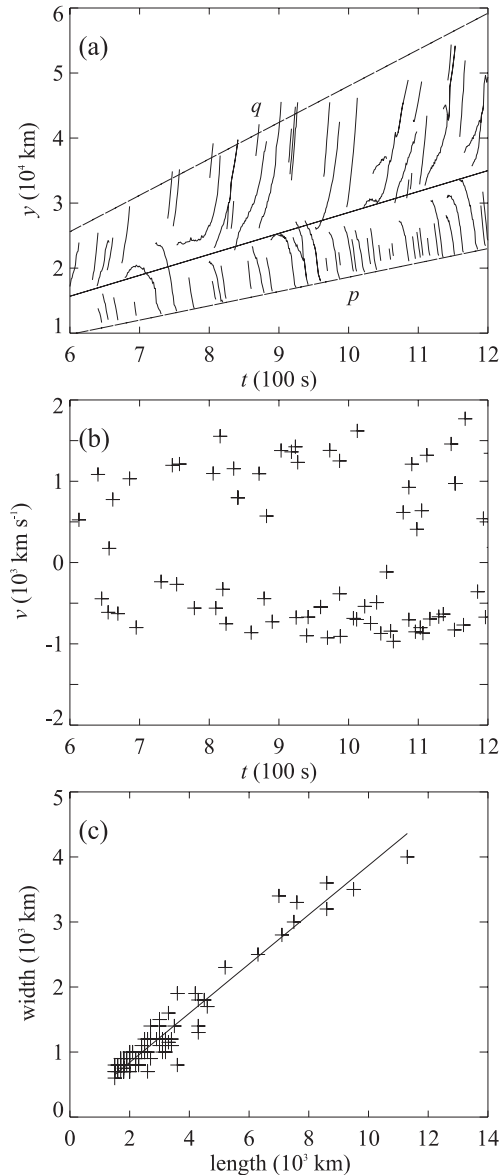


Figure 13. Kinematics of individual plasmoids inside the CS with two dashed lines in panel (a) specifying the upper (q) and the lower (p) ends. The thin curves in panel (a) plot variations of the heights of individual plasmoids versus time. The average velocity of each plasmoid recognized at different times is plotted in (b), and the relation of W to L of each plasmoid is shown in (c). The solid line is the linear fitting to the relation.

in reality. Two thick dashed lines display, respectively, the heights of the upper and the lower tips, q and p , of the CS at different times. They constitute the boundaries of the region where plasmoids are appearing. Those thin solid curves in Fig. 13(a) describe variations of locations of individual plasmoids versus time, and Fig. 13(b) displays velocities of these plasmoids before they leave the CS. On average, each plasmoid moves upward at speeds of about 10^3 km s^{-1} , or moves downward at about 600 km s^{-1} . These velocities are consistent with those observed by Kim et al. (2005), Lin et al. (2005) and Nishizuka et al. (2010), but apparently faster than those observed by Ohyama & Shibata (1998), McKenzie & Hudson (1999), Savage et al. (2010) and Savage & McKenzie (2011).

Furthermore, the aspect ratio of the scale of each plasmoid is also an interesting parameter that is worth studying. It is straight-

forward to measure it as the plasmoid moves in the CS. Fig. 13(c) plots the correlation of the width (W) to the length (L) of the plasmoid (individual crosses), and the solid line is the linear fitting to the results, which suggests that the aspect ratio of plasmoids is approximately 2.

4.5 Width (or thickness) of the CS

A CS of finite length is developed in the eruption shown in our numerical experiments. Therefore, it is necessary to measure its width or thickness in order to compare with observations, which indicated that the CME/flare CS could be thicker than 10^4 km (e.g. see Lin & van Ballegooijen 2005; Lin et al. 2007, 2009; Ciaravella & Raymond 2008 and references therein).

The results of our experiments indicate that the thickness of the CS changes over a large range. The thinnest part of the CS at $t = 30 \text{ min}$ is only about 200 km thick, which is at least 20 times less than the observational values (e.g. see also Lin et al. 2010; Savage et al. 2010), but this value is about 15 times larger than the size of minimum grids in the vicinity of the CS. Therefore, the evolution of the CS in our experiments is always dominated by the physical resistivity because the numerical resistivity becomes important only when the width of the CS spans a couple of grid cells. The thickness of the CS at the place where the biggest plasmoid appears reaches up to 10^4 km , which is in agreement with the observational results for the CS. At around $t = 30 \text{ min}$, the average span between two slow-mode shocks near the upper tip of the CS is about $(3-6) \times 10^3 \text{ km}$. We noticed that as the CS becomes filled with plasmoids and turbulence structures, its thickness appears larger than when no plasmoids or turbulence are present. This implies broadening the CS by plasmoids and turbulence as suggested by Lin et al. (2007, 2009). On the other hand, we also noticed the characteristics of time-dependent Petschek-type reconnection developing in the experiments that may also cause the CS to broaden as indicated by Lin et al. (2009). Some results of this work displayed in previous sections manifest apparent turbulent features in the region between two Petschek shocks as well. Therefore, it is very likely that both turbulence and the Petschek slow-mode shocks govern the scale of the CS during the CME/flare process in a joint fashion. More investigations on this issue are surely necessary in the future.

The above results demonstrate processes that could explain the observed thickness of the flare/CME CS, while at the same time showing that structure is simultaneously able to develop on much shorter length scales. The separation of scales in our simulations is modest compared to the corona because of limitations in computing power, and it remains an open and important question if and how structure is able to develop down to the much smaller collisionless length scales (see e.g. Shepherd & Cassak 2010; Huang, Bhattacharjee & Sullivan 2011).

5 CONCLUSIONS

We studied magnetic reconnection in a CME/flare CS by performing a set of numerical experiments on the basis of the catastrophe model of the solar eruption (Forbes & Isenberg 1991; Isenberg et al. 1993; Lin & Forbes 2000). Before the simulation began, the equilibrium in the configuration including a current-carrying flux rope was tested numerically according to the equilibrium curve of the flux rope given by Isenberg et al. (1993) in the framework of the analytic solution. Five cases listed in Table 1 were tested, and the system in four cases turns out to be in equilibrium eventually although a small deviation in the flux rope location was found from that given by the

analytic solution. The configuration in case 5 is not in equilibrium, and the dynamic evolution in the system commences immediately at the beginning of the experiment.

The output of the test for the first four cases indicated that, in the range of parameters given in Table 1, the system could evolve quasi-statically as the boundary condition changes slowly, and the loss of equilibrium in the system may take place when the critical state is reached. To save the computational resources, we did not start our experiment from the configuration in equilibrium. Instead, we commence to simulate disrupting of the configuration from the state as described in case 5 since the focus of this work is mainly on the reconnecting CS in the eruption. The mesh and AMR strategy were set up so that small-scale features of the reconnection process could be incorporated to the overall evolution of magnetic structure (Ziegler 2005, 2008). This allows us to monitor the global evolution of the system when detailed features in the reconnecting CS are carefully studied, and meanwhile, the numerical diffusion could be reduced efficiently. The evolution in the system is straightforward as expected.

Since the experiment starts from the state of non-equilibrium, the flux rope begins to rise quickly from the very beginning, a fast-mode shock appears in front of it, propagating outward and forming a crescent-shaped front. A dimming region of lower density can be seen between the fast shock and the flux rope. At the same time, a CS forms behind the flux rope about 120 s after the initiation of the experiment and grows continuously in the process. Basically, the global evolution roughly duplicates some observational features in the eruption and the results of previous theoretical and numerical works (e.g. see Mei & Lin 2008; Wang, Shen & Lin 2009 and references therein), but our simulations allow us to capture structure at smaller scales.

The main results of this work are summarized as follows.

(1) The CS does not exist before the eruption, but rather is created when the magnetic configuration is highly stretched by the disruption. Therefore, all the processes occurring inside the sheet commence dynamically from the very beginning. This is different from many previous works on reconnection that were initiated from a pre-existing CS.

(2) In the early stage of the development, the length of the CS increases from 0 to $0.11L_0$ and its thickness remains unchanged at roughly $2 \times 10^{-3}L_0$. In this stage, the development of the CS occurred smoothly, so that its length increases and it develops into a Sweet–Parker sheet. It is interesting that no instability feature appears in the sheet as its aspect ratio exceeded 2π which is the threshold for the tearing mode instability in the framework of the linear theory (Furth et al. 1963). This stage ends as the CS length exceeds $0.11L_0$, and its thickness remains roughly at $2 \times 10^{-3}L_0$, and the aspect ratio exceeds 55. Formation of the first magnetic island or plasmoid in the CS marks the initiation of the tearing mode. What is important about this result is that the tearing mode does not occur in a CS until the aspect ratio of the CS exceeds 50 even if the CS is in the dynamic progress. The same result had been obtained for the CS that is initially static (Loureiro et al. 2007; Ni et al. 2010; Shen et al. 2011). This indicates that magnetic reconnection needs to go through a slow stage in resistive MHD no matter whether the CS configuration is initially in equilibrium or in the progress of fast evolution.

(3) Following the formation of the CS, it takes about 255 s for the first magnetic island to form, the second one was created 79 s after the first one and the third appeared 21 s following the second. This suggests that the plasmoid is produced in an accelerating fashion,

which manifests the non-linear property of the tearing mode in the later stage and provides strong support of the result of the analytic studies by Shibata & Tanuma (2001). The non-linear stage of the tearing mode is also known as the plasmoid instability (e.g. see Huang et al. 2010; Shen et al. 2011 and references therein). As expected, formation of the plasmoid accelerates the reconnection process apparently.

(4) An individual plasmoid even includes internal structures. The electric current existing in the plasmoid consists of two components: a thin shell and a core, and that in the core is obviously stronger than that in the shell. This is probably due to the fractal behaviours of the turbulent plasmoid (Shibata et al. 1995). Most of the plasmoids move inside the CS with acceleration, and merging among individual plasmoids occurs occasionally. The aspect ratio of the plasmoid scale is about 2.

(5) As shown by Shen et al. (2011), two groups of plasmoids in the reconnection outflow are observed to flow along the CS in opposite directions, one group flows upward and another one flows downward, and flowing upward moves apparently faster than flowing downward. Unlike the situation studied by Shen et al. (2011), the plasmoids flowing upward eventually leaves the CS and enters the CME bubble together with the reconnection outflow. Interaction between the plasmoid and magnetic structure inside the bubble (see the upper part of Fig. 10c) yields the further diffusion of the magnetic field and the plasma flow, and results in a hotter and denser shell of the CME bubble as suggested by Lin et al. (2004) and Lin & Soon (2004). Such interactions may even give rise to the temperature in the shell higher than that in the CS. However, this result might be different if radiative cooling were included in the simulation.

(6) Looking into the plasma flow and magnetic structures around the CS, we see the characteristics of the Petschek-type reconnection (see Fig. 11c). The plasma flow pattern and the magnetic field in that region manifest clearly the slow-mode shock of the Petschek type. This is, however, different from the result of the standard theory of the Petschek reconnection, which predicted that the angle spanning between two slow shocks is about 7° , the angle measured in our experiments ranges from 6:5 to 14:1. We ascribed this further expansion of the region between the slow shocks to the turbulence of the plasma in the region. Therefore, broadening of the reconnecting CS could be due to the combined effect of the turbulence and the development of the slow-mode shock (see also discussions of Lin et al. 2008, 2009). Since the Petschek-type reconnection itself is still an open question in the solar physics and plasma physics communities (e.g. see Biskamp 1986; Forbes & Priest 1987; Yokoyama & Shibata 1994; Kulsrud 2001; Drake et al. 2006; Baty, Priest & Forbes 2009; Zweibel & Yamada 2009; Liu, Drake & Swisdak 2012 and references therein), more effort in studying the role of the Petschek-type reconnection in causing solar eruptive phenomena is necessary.

ACKNOWLEDGMENTS

We are grateful to T. G. Forbes and L. Ni for valuable discussions. We would like to thank the editor and an unknown referee as well for the useful comments made on the manuscript. This work was supported by the Program 973 grant 2011CB811403, the NSFC grant 10873030, and the CAS grants 2011T2J01, 2010Y2JB16 and KJCX2-EW-T07 to YNAO. JL and NAM acknowledge support from NASA grant NNX11AB61G and NSF SHINE grant AGS-1156076 to SAO. The NIRVANA v3.5 code was developed by Udo Ziegler at the Leibniz-Institut für Astrophysik Potsdam.

Calculations in this work were completed with the help of the HPC Center, Kunming Institute of Botany, CAS.

REFERENCES

- Bárta M., Vršnak B., Karlický M., 2008, *A&A*, 477, 649
 Bárta M., Büchner J., Karlický M., Kotrč P., 2011, *ApJ*, 730, 47
 Baty H., Priest E. R., Forbes T. G., 2009, *Phys. Plasmas*, 16, 060701
 Bhattacharjee A., Yuan Y., 1995, *ApJ*, 449, 739
 Bhattacharjee A., Huang Y.-M., Yang H., Rogers B., 2009, *Phys. Plasmas*, 16, 112102
 Biskamp D., 1986, *Phys. Fluids*, 29, 1520
 Ciaravella A., Raymond J. C., 2008, *ApJ*, 686, 1372
 Drake J. F., Swisdak M., Schoeffler K. M., Rogers B. N., Kobayashi S., 2006, *Geophys. Res. Lett.*, 33, 13105
 Forbes T. G., 1988, *Sol. Phys.*, 117, 97
 Forbes T. G., 1990, *J. Geophys. Res.*, 951, 11919
 Forbes T. G., 1991, *Geophys. Astrophys. Fluid Dyn.*, 62, 15
 Forbes T. G., Isenberg P. A., 1991, *ApJ*, 373, 294
 Forbes T. G., Lin J., 2000, *J. Atmos. Sol.-Terr. Phys.*, 62, 1499
 Forbes T. G., Malherbe J. M., 1991, *Sol. Phys.*, 135, 361
 Forbes T. G., Priest E. R., 1984, *Sol. Phys.*, 94, 315
 Forbes T. G., Priest E. R., 1987, *Rev. Geophys.*, 25, 1583
 Forbes T. G., Priest E. R., Isenberg P. A., 1994, *Sol. Phys.*, 150, 245
 Furth H. P., Killeen J., Rosenbluth M. N., 1963, *Phys. Fluids*, 6, 459
 Huang Y.-M., Bhattacharjee A., Zweibel E. G., 2010, *Phys. Plasmas*, 17, 055707
 Huang Y.-M., Bhattacharjee A., Sullivan B. P., 2011, *Phys. Plasmas*, 18, 072109
 Isenberg P. A., Forbes T. G., Demoulin P., 1993, *ApJ*, 417, 368
 Karlický M., Bárta M., 2011, *ApJ*, 733, 107
 Karlický M., Bárta M., Nickeler D., 2012, *A&A*, 541, A86
 Kim Y.-H., Moon Y.-J., Cho K.-S., Bong S.-C., Park Y. D., 2005, *ApJ*, 635, 1291
 Ko Y.-K., Raymond J. C., Lin J., Lawrence G., Li J., Fludra A., 2003, *ApJ*, 594, 1068
 Kulsrud R. M., 2001, *Earth Planets Space*, 53, 417
 Lin J., 2002, *Chin. J. Astron. Astrophys.*, 2, 539
 Lin J., Forbes T. G., 2000, *J. Geophys. Res.*, 105, 2375
 Lin J., Soon W., 2004, *New Astron.*, 9, 611
 Lin J., van Ballegoijen A. A., 2002, *ApJ*, 576, 485
 Lin J., van Ballegoijen A. A., 2005, *ApJ*, 629, 582
 Lin J., Forbes T. G., Isenberg P. A., 2001, *J. Geophys. Res.*, 106, 25053
 Lin J., Raymond J. C., van Ballegoijen A. A., 2004, *ApJ*, 602, 422
 Lin J., Ko Y.-K., Sui L., Raymond J. C., Stenborg G. A., Jiang Y., Zhao S., Mancuso S., 2005, *ApJ*, 622, 1251
 Lin J., Li J., Forbes T. G., Ko Y.-K., Raymond J. C., Vourlidas A., 2007, *ApJ*, 658, L123
 Lin J., Cranmer S. R., Farrugia C. J., 2008, *J. Geophys. Res.*, 113, A11107
 Lin J., Li J., Ko Y.-K., Raymond J. C., 2009, *ApJ*, 693, 1666
 Lin J., Li J., Ko Y.-K., Raymond J. C., 2010, in Cranmer S. R., Hoeksema J. T., Kohl J. L., eds, *ASP Conf. Ser. Vol. 428, Understanding a Peculiar Solar Minimum*. Astron. Soc. Pac., San Francisco, p. 177
 Litvinenko Y. E., 1996, *ApJ*, 462, 997
 Liu Y.-H., Drake J. F., Swisdak M., 2012, *Phys. Plasmas*, 19, 022110
 Loureiro N. F., Cowley S. C., Dorland W. D., Haines M. G., Schekochihin A. A., 2005, *Phys. Rev. Lett.*, 95, 235003
 Loureiro N. F., Schekochihin A. A., Cowley S. C., 2007, *Phys. Plasmas*, 14, 100703
 Mackay D. H., van Ballegoijen A. A., 2009, *Sol. Phys.*, 260, 321
 McKenzie D. E., 2000, *Sol. Phys.*, 195, 381
 McKenzie D. E., Hudson H. S., 1999, *ApJ*, 519, L93
 Mei Z., Lin J., 2008, *New Astron.*, 13, 526
 Murphy N. A., 2010, *Phys. Plasmas*, 17, 112310
 Murphy N. A., Sovinec C. R., Cassak P. A., 2010, *J. Geophys. Res.*, 115, A09206
 Ni L., Germaschewski K., Huang Y.-M., Sullivan B. P., Yang H., Bhattacharjee A., 2010, *Phys. Plasmas*, 17, 052109
 Nishida K., Shimizu M., Shiota D., Takasaki H., Magara T., Shibata K., 2009, *ApJ*, 690, 748
 Nishizuka N., Takasaki H., Asai A., Shibata K., 2010, *ApJ*, 711, 1062
 Ohya M., Shibata K., 1997, *PASJ*, 49, 249
 Ohya M., Shibata K., 1998, *ApJ*, 499, 934
 Øieroset M., Phan T. D., Fujimoto M., Lin R. P., Lepping R. P., 2001, *Nat.*, 412, 414
 Orlanski I., 1976, *J. Comput. Phys.*, 21, 251
 Petschek H. E., 1964, in Hess W. N., ed., *Proc. AAS-NASA Symp. Vol. 50, The Physics of Solar Flares*. NASA, Science and Technical Information Division, Washington, DC, p. 425
 Priest E., Forbes T., 2000, *Magnetic Reconnection*. Cambridge Univ. Press, Cambridge
 Priest E. R., Forbes T. G., 2002, *A&ARv*, 10, 313
 Raymond J. C., Ciaravella A., Dobrzycka D., Strachan L., Ko Y.-K., Uzzo M., Raouafi N.-E., 2003, *ApJ*, 597, 1106
 Riley P., Lionello R., Mikić Z., Linker J., Clark E., Lin J., Ko Y.-K., 2007, *ApJ*, 655, 591
 Sato T., 1979, *J. Geophys. Res.*, 84, 7177
 Savage S. L., McKenzie D. E., 2011, *ApJ*, 730, 98
 Savage S. L., McKenzie D. E., Reeves K. K., Forbes T. G., Longcope D. W., 2010, *ApJ*, 722, 329
 Shen C., Lin J., Murphy N. A., 2011, *ApJ*, 737, 14
 Shepherd L. S., Cassak P. A., 2010, *Phys. Rev. Lett.*, 105, 015004
 Shibata K., Tanuma S., 2001, *Earth Planets Space*, 53, 473
 Shibata K., Masuda S., Shimojo M., Hara H., Yokoyama T., Tsuneta S., Kosugi T., Ogawara Y., 1995, *ApJ*, 451, L83
 Strauss H. R., 1988, *ApJ*, 326, 412
 Ugai M., Tsuda T., 1979, *J. Plasma Phys.*, 22, 1
 Vršnak B., Sudar D., Ruždjak D., 2005, *A&A*, 435, 1149
 Wang H., Shen C., Lin J., 2009, *ApJ*, 700, 1716
 Wood P., Neukirch T., 2005, *Sol. Phys.*, 226, 73
 Yamada M., Ren Y., Ji H., Breslau J., Gerhardt S., Kulsrud R., Kuritsyn A., 2006, *Phys. Plasmas*, 13, 052119
 Yokoyama T., Shibata K., 1994, *ApJ*, 436, L197
 Yokoyama T., Shibata K., 2001, *ApJ*, 549, 1160
 Ziegler U., 2004, *J. Comput. Phys.*, 196, 393
 Ziegler U., 2005, *Comput. Phys. Commun.*, 170, 153
 Ziegler U., 2008, *Comput. Phys. Commun.*, 179, 227
 Ziegler U., 2011, *J. Comput. Phys.*, 230, 1035
 Zweibel E. G., Yamada M., 2009, *ARA&A*, 47, 291

This paper has been typeset from a $\text{\TeX}/\text{\LaTeX}$ file prepared by the author.